C. R. Mecanique 347 (2019) 101–113

Contents lists available at ScienceDirect

Comptes Rendus Mecanique

www.sciencedirect.com

A reduced-order model manifold technique for automated structural defects judging using the PGD with analytical validation

Chady Ghnatios [a,*], Ghazi Asmar [a], Elie Chakar [b], Charbel Bou Mosleh [a]

[a] Notre Dame University-Louaize, Department of Mechanical Engineering, Zouk Mosbeh, PO Box 72, Lebanon
[b] Notre Dame University-Louaize, Department of Civil Engineering, Zouk Mosbeh, PO Box 72, Lebanon

ARTICLE INFO

Article history:
Received 17 August 2018
Accepted 16 November 2018
Available online 23 January 2019

Keywords:
Holes
Complex potentials
Fourier series
Stress concentration
Model reduction
Manifold technique
Proper Generalized Decomposition

ABSTRACT

Automation is conquering new fields on a daily basis. Aiming for faster and more reliable products, industrials as well as researchers are oriented into automation. Non-destructive testing as well as defect quantification is not an exception. In fact, decisions with minimum allowable error are sought in real-time when facing any potential defect. In this work, we suggest a comprehensive method based on model order reduction techniques to judge if a structure shall be salvaged. The real-time decision is based on multidimensional parametric simulation, performed offline, using the Proper Generalized Decomposition (PGD). The PGD is a model order reduction technique that allows circumventing the curse of dimensionality by using domain decomposition. Therefore, the 6D simulation illustrated in this paper is performed within a few minutes on a standard laptop. Later on, a stress concentration manifold is built and used online for decision-making. The manifold is validated on a few selected solutions solved analytically using an analytical procedure. The aforementioned procedure is developed, in this paper, to calculate the tangential stress around circular holes of different sizes, in an infinite isotropic plate containing any number of holes and subjected to in-plane pressure loading at the tip of the infinite plate. The procedure is based on determining two Muskhelishvili complex potentials in terms of complex Fourier series, and applying the Schwartz alternating method repeatedly until the boundary conditions on the contour of every hole are satisfied.

1. Introduction

Defects quantification as well as non-destructive testing are active research topics. Moreover, it is well known that holes in stressed structures are stress raisers, which, if not accounted for, may lead to catastrophic failures of the structure. Moreover, the presence of multiple interacting holes may lead to complicated and counter-intuitive results. Such a phenomenon is encountered, for example, when military helicopters or aircrafts are hit with flakes or penetrating bullets. Therefore, stress concentration around holes became of high interest in military applications, aiming to understand the effect of penetrating bullets on the structure and the ability of the latter to withstand in-flight manoeuvers. On the other hand, aiming for faster and more reliable decision making techinques, engineers develop real-time model-based and/or data-based decision-making

* Corresponding author.
E-mail address: cghnatios@ndu.edu.lb (C. Ghnatios).

https://doi.org/10.1016/j.crme.2018.11.003
1631-0721/

techniques. In this work, we expose a real-time decision-making technique for judging the threat created by defects in general, and show an application on structural defects, such as holes, on the general sustainability of the structure. The threat of holes in airplanes should be assessed in real-time, sometimes on a battlefield, using simple measurements like the hole diameters and the gap between the holes, before attempting to takeoff. Therefore, numerous studies are undertaken to estimate the stress concentrations around holes, either numerically or analytically [2,26].

In this work, we aim to build a decision manifold. Therefore, we model the holes using the structure's geometrical properties (diameter, gap between the holes and thickness of the modeled part) as extra coordinates of the problem. Such an approach shall provide an abacus containing all the solutions for all possible combinations of these parameters. However, adding extra parameters increases the dimensionality of the problem, which becomes a 6D problem, three physical coordinates and three parametric ones. Thus, model order reduction techniques appear as an appealing approach to take [6,7,4]. These techniques aim to circumvent the curse of dimensionality by solving the full dimensionality problem, 6D for instance, as a sequence of lower-dimensionality problems (2D of 1D for example) [10]. Many model order reduction techniques are qualified as "a posteriori" techniques, which means that they require to solve few full-dimensionality problems before building the reduced-order model. However, the Proper Generalized Decomposition (PGD) is an "a priori" model order reduction technique [1]. In fact, the PGD will build the reduced-order model without solving the full-dimensionality problem as a sequence of lower-dimensionality ones [1,11].

Once the multidimensional 6D solution is available, a post-processing of the solution provides the stress concentration values for any hole diameter, gap or plate thickness. This leads to a construction of a 3D stress concentration manifold where the dimensions are the diameter, the gap, and the plate's thickness. The manifold learning approach is already popular and integrated in many scientific applications [18,19]. Numerous algorithms are being developed nowadays to build manifolds, such as the Kernel Principal Components Analysis (KPCA) [24], Local Linear Embedding (LLE) [23] and many others. Recent applications combined the PGD with manifold learning techniques, opening up unprecedent possibilities of performing real-time simulations unimaginable using classical techniques [15]. In this work, the developed manifold provides a simple real time simulation-based decision-making criterion for the severity of a given structural defect, by comparing a stress concentration threshold to a stored manifold, for example. This approach can be easily used by simple workers without any scientific background, or integrated in a smartphone application, for example.

Moreover, in this paper we provide an analytical method to compute the stress concentration around multiple interacting holes, along with, in Appendix B, the analytical method used to calculate the stress field in an infinite isotropic plate subjected to in-plane loading at the plate ends. The plate may contain any finite number of non-intersecting circular holes of different sizes. The holes may be disposed in any manner within the plate and the loading may be at any angle α with respect to the horizontal direction. The theoretical treatment of the method, which is based on a complex Fourier series approximation of two Muskhelishvili complex potentials, is presented in [2], which also contains a literature review of relevant work that has been achieved in this regard beginning with [20] and covering several notable papers such as [17,21]. Previous works using the Schwartz alternating method have been published in [25,26,22].

The results for plates with various holes diameters and relative positions are also presented in this work comparing both the PGD method and the analytical technique, as a validation of the resulting manifold in section 5.

2. Modeling of the problem

From military investigations, flakes and penetrating bullets generate often circular holes in helicopters, rarely elliptical ones. Thus, in this work, for the sake of simplicity and without loss of generality, we are modeling the holes as circles having a diameter D inside an infinite plate. Moreover, airplane windows can be approximated by circular holes in fuselage plates. To avoid any edge effects, the plate edges in the simulation are located at a distance at least equal to 10 times the diameter of the holes [17,25].

Neglecting any volumetric loading in the simulated domain, the governing equilibrium equation modeling the displacement in a plate can be written as [3]:

$$\nabla \cdot \sigma = 0, t \tag{1}$$

where σ is the Cauchy stress tensor. Assuming linear elastic behavior, one may write $\sigma = \mathcal{K}\epsilon$, where $\mathcal{K}$ is the elasticity tensor and ϵ the strain one. Noting the displacement vector by $\mathbf{u} = (u, v, w)$, the strain tensor is therefore written as:

$$\epsilon = \frac{1}{2}\left(\nabla \mathbf{u} + \nabla \mathbf{u}^{\intercal}\right) \tag{2}$$

Combining Eqs. (2) and (1) and integrating by part, one may reach the final weak form of the governing differential equation to solve:

$$\frac{1}{4}\int_{\Omega} \left(\nabla \mathbf{u}^* + \nabla \mathbf{u}^{*\intercal}\right)^{\intercal} \cdot \mathcal{K} \cdot \left(\nabla \mathbf{u}^* + \nabla \mathbf{u}^{*\intercal}\right) \mathrm{d}\Omega = \int_{\partial\Omega} \mathbf{u}^* \cdot \mathbf{F} \mathrm{d}\Omega \tag{3}$$

Solving equation (3) leads to the displacement at each point of the simulated domain under specified external loads and boundary conditions, $\mathbf{F}$ being the surface forces and $\mathbf{u}^*$ the test function. For instance, the problem discussed in this

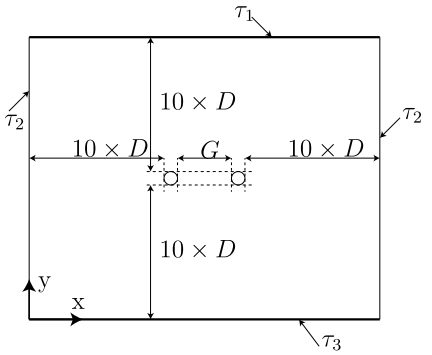

Fig. 1. Simulated plate.

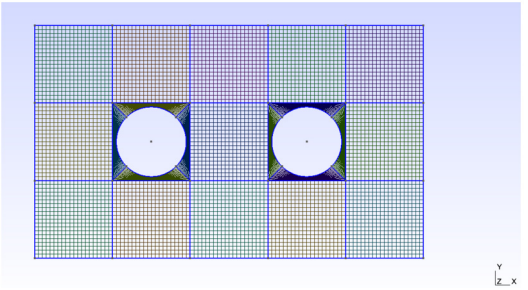

Fig. 2. The domain (q, r, s) used for solving the 6D problem. Each square has 1×1 as dimensions.

work is solved in a plate domain of constant thickness t and in-plane dimensions of $(22D + G) \times (21D)$ as illustrated in Fig. 1, where G is the gap between two neighboring holes. The imposed boundary conditions in this problem are a constant displacement U_0 applied parallel to the y-axis at τ_1 and free ends at τ_2, as well as a fixed boundary with zero displacements, $\mathbf{u} = \mathbf{0}$ for instance, at τ_3. To solve this problem in a general manner and construct an abacus of solutions, also known as a computational vademecum [1,7], one has to solve the problem for each combination of the values of D, G, and the thickness of the part t. That is where the use of the PGD appears to be an appealing approach to take, since the PGD allows circumventing the curse of dimensionality by decomposing the full-dimensionality problem into a sequence of lower-dimensionality ones [6]. Therefore, we add the parameters D, G, and t as extra coordinates of the problem, leading therefore to a $6D$ problem to solve.

Since t, D, as well as G are now problem parameters and therefore extra coordinates, a geometrical transformation should be defined from the parametric real domain (x, y, z) into a fixed-dimension calculation domain (q, r, s) [11,14,13]. In fact, D, G, and t do not appear explicitly in the governing equation (3), and the dimensions of the calculation domain are not fixed. Therefore, the geometrical transformation will incorporate these extra coordinates in the weak form of the problem, and lead to a domain of fixed dimensions that can be easily meshed. For instance, the dimensions of the reference fixed domain used in this work (q, r, s) are $5 \times 3 \times 1$ as illustrated in Fig. 2, illustrating the in-plane mesh. The geometrical transformation transforming the (x, y, z) domain into the reference (q, r, s) one writes:

$$\begin{cases} q \in [0;1], x = 9.5D \cdot q \\ q \in [1;2], x = 9.5D + 2D \cdot (q-1) \\ q \in [2;3], x = 11.5D + (q-2) \cdot G \\ q \in [3;4], x = 11.5D + G + 2D \cdot (q-3) \\ q \in [4;5], x = 13.5D + G + 9.5D \cdot (q-4) \\ \\ r \in [0;1], y = 9.5D \cdot r \\ r \in [1;2], y = 9.5D + 2D \cdot (r-1) \\ r \in [2;3], y = 11.5D + 9.5D \cdot (r-2) \\ \\ z = t \cdot s \end{cases} \tag{4}$$

The fixed calculation domain (q, r, s) is defined by the dimensions and shape illustrated in Fig. 2. A refined mesh around the holes ensures a good estimation of the stress concentrations around them. The transformation depicted in Eq. (4) leads

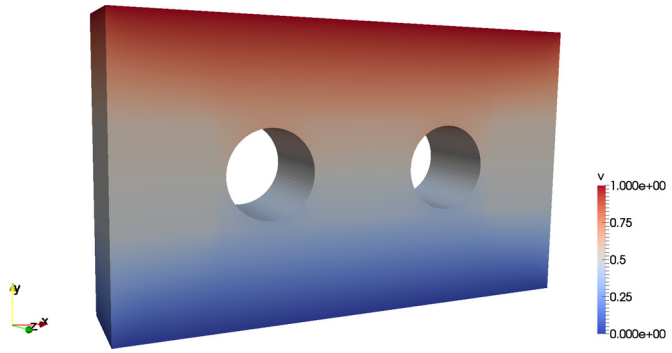

Fig. 3. The displacements in m for $U_0 = 1$ illustrated in the calculation domain (q, r, s).

to a easily separable Jacobian matrix, which is suitable for a separated representation framework, like the PGD used in this work [5].

Combining Eqs. (4) and (3) leads to a formulation where the extra parameters of the problem are included in the problem's model. Solving the resulting problem in the (q, r, s) reference domain, while considering the thickness t, the diameter D, and the gap G as problem coordinates leads to a 6D abacus. This abacus contains the full 3D solutions for any value of D, G, and t inside a chosen domain interval. Eventually, solving this problem using classical numerical techniques leads to a prohibitive and unrealistic calculation time, compromising the feasibility of this approach. However, the PGD solves for the displacement vector field $\mathbf{u}$ as a sum of product of functions such as:

$$\mathbf{u} = \sum_{i=1}^{i=N} \begin{pmatrix} X_i(q,r) \cdot S_{xi}(s) \cdot \mathcal{D}_i(D) \cdot \mathcal{G}_i(G) \cdot \mathcal{T}_i(t) \\ Y_i(q,r) \cdot S_{yi}(s) \cdot \mathcal{D}_i(D) \cdot \mathcal{G}_i(G) \cdot \mathcal{T}_i(t) \\ Z_i(q,r) \cdot S_{zi}(s) \cdot \mathcal{D}_i(D) \cdot \mathcal{G}_i(G) \cdot \mathcal{T}_i(t) \end{pmatrix} \tag{5}$$

where X_i, Y_i and Z_i are the *in-plane* components (q, r) of the displacement vector $\mathbf{u}$, while S_{xi}, S_{yi} and S_{zi} are the functions of the *out-of-plane* components of $\mathbf{u}$. In this work, we choose to decompose the 3D domain into a sequence of 2D (q, r) $\times$ 1D s to avoid the separation of the domain containing circular holes. In fact, the circles can be separated into a sequence of 1D functions at the expense of increasing the problem's complexity and calculation time. Such separation may therefore increase the calculation time above the needed time to solve the 2D problem. For a detailed construction of the parametric 6D solution within the PGD framework, the reader may refer to the following publications and the references therein [6,7].

The full 6D solution in question is obtained using the PGD algorithm in the form depicted in Eq. (5) on a core i7 and 8 GB RAM laptop. The PGD algorithm is detailed in Appendix A. Eventually, the problem calculation time highly depends on the 2D mesh and not on the parameters or thickness mesh, since the calculation time of 1D solutions is negligible with respect to a 2D one. Typically, for a mesh of 8639 nodes in the in-plane dimension (q, r), 60 nodes in the thickness direction s, 500 nodes for G, 100 nodes for D and 50 nodes for t, it takes about 36 min of calculation for a residual reduction factor of about 10^{-3}, corresponding to 50 PGD products of functions ($N = 50$ in equation (5)). Eventually, increasing the mesh in the in-plane dimension may increase the calculation time up to about a few hours.

In the next section, we detail the post-processing of the 6D parametric solution obtained using the PGD and the construction of the stress concentration manifold around the holes.

3. Post-processing the 6D solution

In this section, we post-process the solution obtained in section 2 and reduce it to an abacus offering a virtual chart that can be used in real time for decision-making as a manifold technique. To explore the 6D solution, a pxdmf file is used along with a PGD separated representation plugin for Paraview. Using $U_0 = 1$ m (making use of the linearity of the domain), Fig. 3 shows the displacement magnitude $\|\vec{\mathbf{u}}\|$ in the (q, r, s) domain, whereas Fig. 4 illustrates the same displacement magnitude in the real (x, y, z) domain. The reader may note that all the plate figures in this section are chosen as $D = 0.05$ m, $G = 0.025$ m, and $t = 0.009$ m for illustrative purposes.

One can also illustrate the deformed shape of the part in the real domain (x, y, z) using the inverse transformation. Fig. 5 illustrates the deformations in the real (x, y, z) domain.

The stress tensor σ at each point of the material can be computed by first calculating the gradients of $\mathbf{u}$ and then using Eq. (2), which leads to:

$$\sigma = \mathcal{K}\epsilon = \mathcal{K} \cdot \frac{1}{2}\left(\nabla \mathbf{u} + \nabla \mathbf{u}^{\intercal}\right) \tag{6}$$

Later on, one may compute the Von Mises effective stress in the domain, as illustrated in Fig. 6. One can also check the stress values around the holes in real-time by changing the values of D, G, or t in a sliding bar as illustrated in Fig. 7, an option offered by the Paraview plugin, leading to a real virtual chart available in real-time.

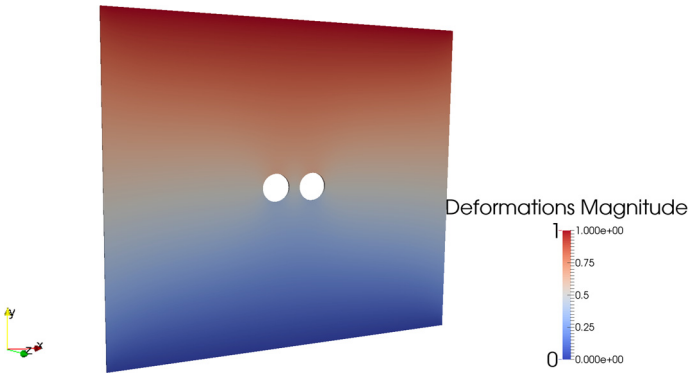

Fig. 4. The displacements in m for $U_0 = 1$ illustrated in the real domain (x, y, z).

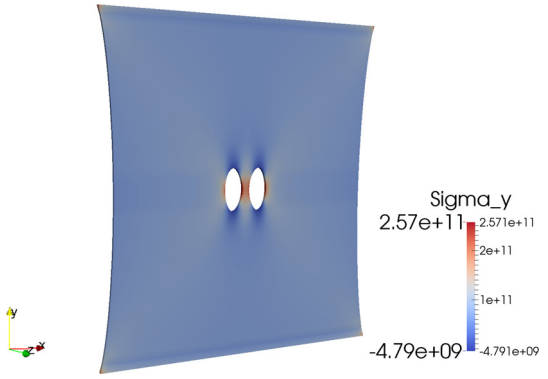

Fig. 5. The deformed part under the action of the imposed boundary conditions in the (x, y, z) domain.

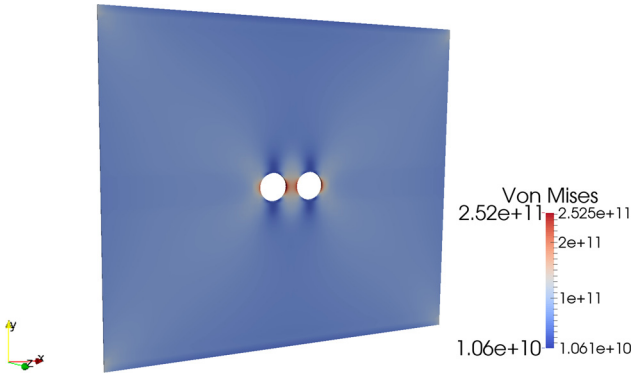

Fig. 6. The Von Mises effective stresses $\sigma_{\text{Von Mises}}$ in Pa, illustrated in the real domain (x, y, z).

In this section, we define the stress concentration factor at the holes **K** in the plates subjected to tension as the maximum in-plane axial stresses in the tensile direction (existing on the hole circumference eventually) divided by the axial average stress existing in a "healthy" plate without holes at the same location:

$$\mathcal{K} = \frac{\sigma_{y_{\max}}}{\sigma_{y_{\text{avg}}}} \tag{7}$$

Fig. 8 illustrates the variation of the stress concentration factor $\mathcal{K}$ as a function of the gap G and of the diameter D of the holes, t being the least influencing variable on the stress concentration values in the chosen simulation domain. Fig. 8, is a straightforward tool for the estimation of the reliability of the structure as well as of the threat created by the hole, using a allowable threshold. For example, if $\mathcal{K}$ is larger than the allowable threshold, which can be set as the factor of safety of the designed part, the studied element shall be salvaged. We note that $\mathcal{K}$ has an increasing tendency with increasing D and decreasing G, which is normal since the holes tend to interact at closer relative distances. One may define a dimensionless number such as D/G. A threshold can also be set on the dimensionless number D/G, for example.

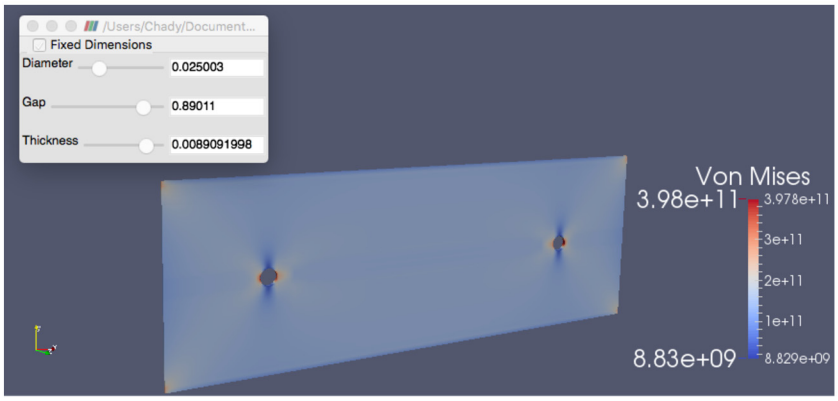

Fig. 7. Variation of the Von Mises effective stresses $\sigma_{\text{Von Mises}}$ in Pa, computed in real-time as a function of D, G, and t.

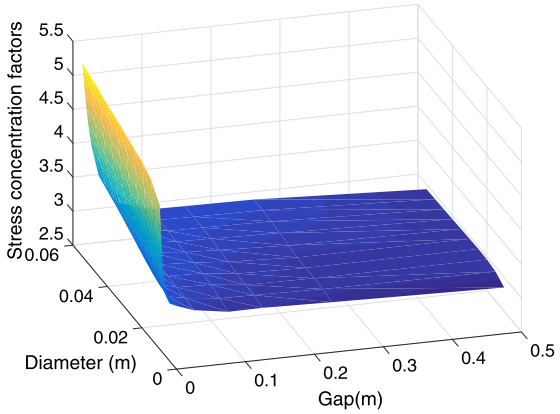

Fig. 8. Variation of the stress concentration factor **K** as a function of D and G for $t = 0.005$ m.

4. The analytical model

Consider an infinite plate containing n circular holes, which may be of different sizes, with respective radii $\rho_1, \rho_2, \ldots, \rho_n$, and centers denoted by $O_1, O_2, \ldots, O_n$. The holes may be disposed in any manner relative to each other within the plate as long as they do not intersect. Let the plate be subjected to a pressure loading of magnitude s^∞ at infinity, at an angle α with respect to the horizontal direction, as shown in Fig. 9(a). It is required to calculate the stress at any point in the plate. In particular, the tangential stress on the contour of any of the holes is sought because it is a measure of the stress concentration around any hole and is an indication of the influence of one hole on the other.

The problem illustrated in Fig. 9(a) is solved by superposing the case in Fig. 9(b), where the plate is subjected to the same remote loading but is hole-free, with the case in Fig. 9(c), where each hole is loaded at its contour with no loading at infinity. In Fig. 9(b), the contours of the circles shown in dashed lines represent "would-be" holes or locations where the holes would exist. In Fig. 9(c), the loads on the periphery of each hole are radial and shear stresses that are, respectively, equal and opposite to those determined from the case in Fig. 9(b), In this way, the boundary conditions on the contour of each hole, i.e. no radial and no shear stresses, are satisfied. Thus, in Figs. 9(b) and 9(c), s_0^i $(i = 1, 2, \ldots, n)$ stand for both the radial and shear stresses in the hole-free plate. The superscript "0" is used to identify a stress in a hole-free plate.

The tangential stress at a point round every hole in Fig. 9(a) is then calculated as the sum of the tangential stresses at the same point in each of the plates in Figs. 9(b) and 9(c). Now the radial, tangential, and shear stresses at any point of the plate in Fig. 9(b) may be determined from:

$$s_r^0 = s^\infty \cdot \left(\cos^2\alpha \cdot \cos^2\theta + \sin^2\alpha \cdot \sin^2\theta + \tfrac{1}{2}\sin(2\alpha) \cdot \sin(2\theta)\right) \tag{8}$$

$$s_\theta^0 = s^\infty \cdot \left(\cos^2\alpha \cdot \sin^2\theta + \sin^2\alpha \cdot \cos^2\theta - \tfrac{1}{2}\sin(2\alpha) \cdot \sin(2\theta)\right) \tag{9}$$

$$s_{r\theta}^0 = \tfrac{s^\infty}{2} \cdot \left(\sin(2\alpha) \cdot \left(\cos^2\theta - \sin^2\theta\right) + \sin(2\theta) \cdot \left(\sin^2\alpha - \cos^2\alpha\right)\right) \tag{10}$$

where θ is the counterclockwise angle between any ρ_i and the horizontal direction, as shown in Fig. 9(a).

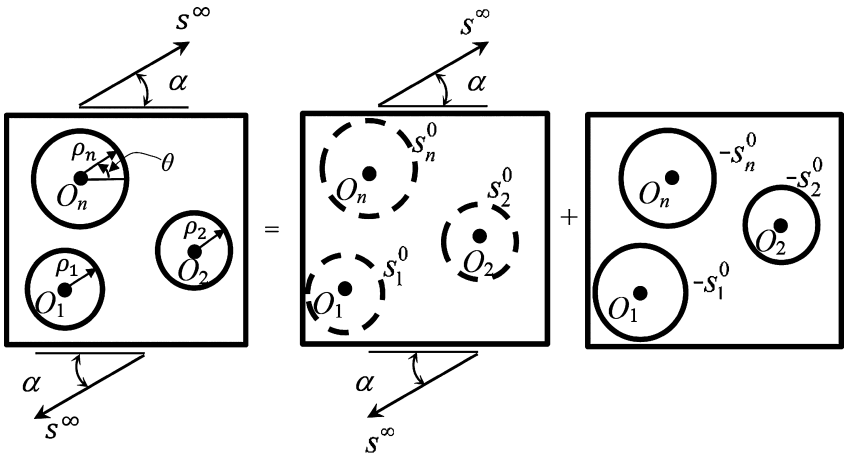

(a) Plate with holes under remote loading.

(b) Hole-free plate under remote loading.

(c) Plate with loading on the contours of the holes.

Fig. 9. Plate with holes under different types of loading.

The stresses at any point in the plate of Fig. 9(c) are determined using the Kolosov–Muskhelishvili equations [22], such as:

$$s_r + s_\theta = 4 \cdot \mathrm{Re}\left[\psi'(z)\right] \tag{11}$$

$$s_\theta - s_r + 2 \cdot \mathrm{i} \cdot s_{r\theta} = 2\left[\bar{z}\psi''(z) + \mathcal{X}''(z)\right] \mathrm{e}^{2\mathrm{i}\theta} \tag{12}$$

where s_r, s_θ, and $s_{r\theta}$ are, respectively, the radial, tangential and shear stresses in the plate of Fig. 9(c), $\mathrm{i} = \sqrt{-1}$, $z = x + \mathrm{i}y$, $\bar{z} = x - \mathrm{i}y$ and Re denotes the real part of a complex number. $\psi(z)$ and $\mathcal{X}(z)$ are two Muskhelishvili complex potentials, and the prime and double primes represent, respectively, the first and second derivatives of the complex potentials with respect to z.

For a plate containing only one hole of radius ρ with s_r and $s_{r\theta}$ being known radial and shear stress loadings specified at the hole boundary, the complex potentials are determined as follows. Let:

$$\psi'(z) = \sum_{k=0}^{\infty} A_k \cdot z^{-k} \text{ and } \mathcal{X}''(z) = \sum_{k=0}^{\infty} B_k \cdot z^{-k} \tag{13}$$

The coefficients A_k and B_k are obtained by expanding the stresses around the contour of the hole in a complex Fourier series. Thus, if s_r and $s_{r\theta}$ are radial and shear stresses applied on the hole contour, i.e. at $r = \rho$, then:

$$(s_r + \mathrm{i}\, s_{r\theta})_{r=\rho} = \sum_{k=-\infty}^{\infty} C_k \cdot \mathrm{e}^{\mathrm{i}k\theta} \tag{14}$$

where the Fourier coefficients are given by:

$$C_k = \frac{1}{2\pi} \int_0^{2\pi} \left((s_r + \mathrm{i}\, s_{r\theta})_{r=\rho}\right) \mathrm{e}^{-\mathrm{i}k\theta} \mathrm{d}\theta \quad (k = 0, \pm 1, \pm 2, \ldots) \tag{15}$$

Now upon substituting $\psi'(z)$ and $\mathcal{X}''(z)$ from Eqs. (13) into the right-hand sides of Eqs. (11) and (12), substituting $(s_r + \mathrm{i}\, s_{r\theta})_{r=\rho}$ from Eq. (14) into the left-hand sides of Eqs. (11) and (12), letting $z = \rho \cdot \mathrm{e}^{\mathrm{i}\theta}$ on the hole boundary, and comparing the coefficients of $\mathrm{e}^{\mathrm{i}k\theta}$ on both sides of Eqs. (11) and (12), one can determine A_k and B_k from the known Fourier coefficients C_k. Therefore, if the plate were to contain one hole only under loading around the hole boundary, the problem would end there.

For a plate containing multiple holes, use is made of the Schwartz alternating method, where the above solution for a plate containing a single hole is repeatedly applied to every hole in the plate until the boundary conditions; no radial and no shear stresses around the periphery of every hole are satisfied. Since the procedure is iterative, the satisfaction of the boundary conditions is, of course, approximate and consists of checking after every cycle of loading whether the absolute values of the maximum (or minimum) radial and shear stresses around every hole are below a set value, sufficiently close to zero. Every cycle of loading brings about a decrease in the radial and shear stresses around every hole so that, after a certain number of cycles, the boundary conditions have effectively been satisfied.

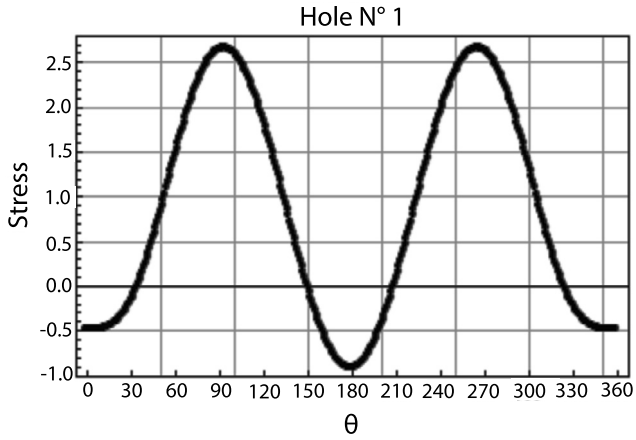

Fig. 10. Tangential stress variation around the left or right hole in a plate with two holes disposed and loaded horizontally, as a function of the angle θ on the hole.

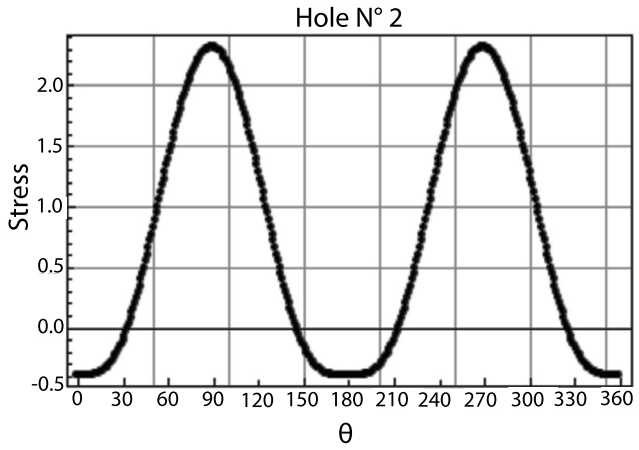

Fig. 11. Tangential stress variation around the center hole in a plate with three holes disposed and loaded horizontally, as a function of the angle θ on the hole.

This process is described in Appendix B, which is at the heart of the Schwartz alternating method. This process is implemented in a Mathematica computer code to provide an analytical validation of the constructed manifold.

4.1. Results and discussion

The Schwartz alternating method illustrated in Appendix B is used to calculate the tangential stress around holes in plates containing 2, 3, and 4 holes. All loads consist of pressures of magnitude 1 unit of pressure at infinity and at various orientations, making either 0° or 45° with respect to the horizontal direction. In the graphs depicted in this section, the tangential stress around the contour of a hole, which may also be considered as the stress concentration factor, is plotted with respect to the angle θ in degrees as defined in Fig. 9(a). Further, let D_i be the diameter of hole i centered at O_i, and let O_iO_j $(i \neq j)$, be the center-to-center distance between hole i and hole j. Although all of the holes considered in this section are of the same size with $D_i = 1$ unit of length, more numerical results, including consideration of holes of unequal size may be found in [2]. The examples in this section are mainly intended to corroborate the validity of the method.

Fig. 10 depicts the tangential stress around the left hole (hole No. 1) in a plate containing a pair of identical holes whose centers are located on a straight line parallel to the horizontal direction such that $O_1O_2 = 1.7$ units of length. The loading direction is also parallel to the horizontal direction. Due to symmetry, the tangential stress variation around the right hole (hole No. 2) is, of course, the same. It is interesting to note, in this case, that the mutual influence of the holes is such that a stress relief occurs. Indeed, the maximum tangential stress at any point around the contour of any of the holes is less than 3.0, i.e. it is lower than that resulting in a plate containing a single hole of the same size and loaded similarly.

The same is also observed in a plate containing three horizontally aligned holes of the same size as above, with centers, from left to right, denoted by O_1, O_2, and O_3, respectively, with $O_1O_2 = O_2O_3 = 1.7$ units of length, and loaded horizontally. Note that the stress relief is even greater around the center hole as may be seen in Fig. 11.

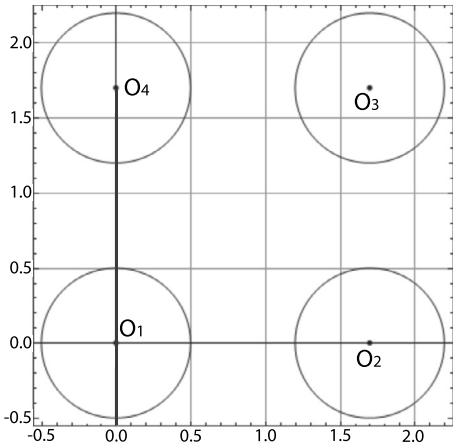

Fig. 12. Four holes arranged in a square configuration.

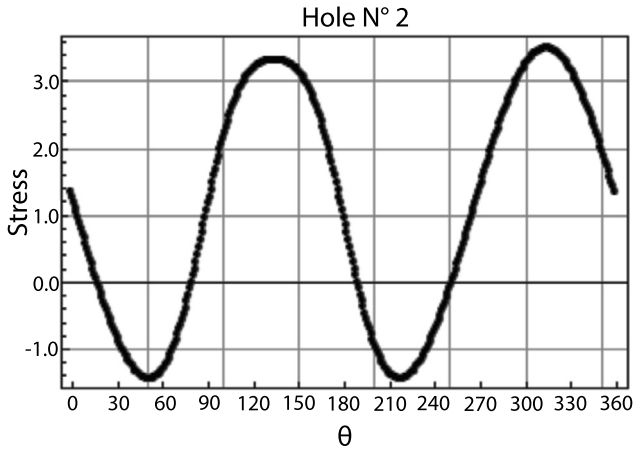

Fig. 13. Tangential stress variation around hole #2 in a plate with a 4-hole square configuration loaded at 45°, as a function of the angle θ.

For the 4-hole square configuration depicted in Fig. 12 with a center-to-center side length of 1.7 units of length and loaded horizontally, the maximum tangential stress around any of the holes approaches 3.0. However, this maximum is exceeded when the applied stress is oriented at 45° with respect to the horizontal direction as may be seen in Fig. 13, which shows a maximum of around 3.6 at close to 330° on the hole contour. The same is true for hole #4, but with the point of maximum stress located at a position close to 135°.

To corroborate the results obtained from the present method, finite element calculations are performed using AERO-S. AERO-S is a finite element computer code developed by Farhat Research Group (FRG) in the Aeronautics and Astronautics Department, at Stanford University, and successfully used in aeronautical research with experimentally proven results [8,9]. The tangential stress contour plots generated from AERO-S for an aligned four-hole configuration are depicted in Fig. 14. These contour plots are for holes with a center-to-center distance equal to 1.7 units of length for any two adjacent holes and loaded at $\alpha = 45°$ with respect to the horizontal direction.

Tables 1 and 2 show the maximum and minimum tangential stresses (a compressive stress has a negative value) and their corresponding locations around the contours of the first and second holes (the left-most hole is hole No. 1) along with their relative errors in a plate containing four holes aligned horizontally as depicted in Fig. 14. As can be seen in Tables 1 and 2, a very good agreement has been obtained between the results generated by the present method and the finite element results obtained using *Farhat Research Group (FRG)*'s software. The relative error of 6.3% shown around hole 2 in Table 1 can be generated by the AERO-S mesh.

Table 1 shows the results for a plate subjected to horizontal loading, while in Table 2 one can find those for a plate subjected to a loading at $\alpha = 45°$ with respect to the horizontal direction. It can be seen from Tables 1 and 2 that a very good agreement is obtained between the results generated by the present method and the AERO-S finite element results. Moreover, it is noted from Table 1 that, for a loading oriented along the horizontal direction $\alpha = 0°$, a stress relief is obtained, similar to the case of two and three holes, whereas, for loading at $\alpha = 45°$, this is not the case, as may be seen

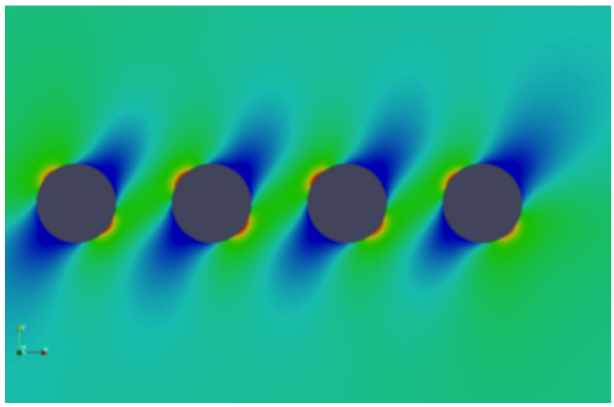

Fig. 14. Tangential stress contour plot generated in a plate containing four aligned holes under a loading oriented by $\alpha = 45°$.

Table 1
Tangential stress values and locations around holes 1 and 2 under horizontal loading ($\alpha = 0°$) as determined by the present method and by AERO-S.

Hole number	Analytical method	AERO-S	Relative error
1	$(\sigma_\theta)_{\max} = 2.583$ at $\theta = 94°, 266°$ $(\sigma_\theta)_{\min} = -0.854$ at $\theta = 180°$	$(\sigma_\theta)_{\max} = 2.585$ at $\theta = 92.34°, 260°$ $(\sigma_\theta)_{\min} = -0.872$ at $\theta = 180°$	0.07% 2%
2	$(\sigma_\theta)_{\max} = 2.265$ at $\theta = 90°, 270°$ $(\sigma_\theta)_{\min} = -0.360$ at $\theta = 180°$	$(\sigma_\theta)_{\max} = 2.353$ at $\theta = 90°, 272.67°$ $(\sigma_\theta)_{\min} = -0.337$ at $\theta = 180°$	3.7% 6.3%

Table 2
Tangential stress values and locations around holes 1 and 2 under horizontal loading ($\alpha = 45°$) as determined by the present method and by AERO-S.

Hole number	Analytical method	AERO-S	Relative error
1	$(\sigma_\theta)_{\max} = 3.731$ at $\theta = 328°$ $(\sigma_\theta)_{\min} = -1.605$ at $\theta = 38°$	$(\sigma_\theta)_{\max} = 3.748$ at $\theta = 327.03°$ $(\sigma_\theta)_{\min} = -1.619$ at $\theta = 36.2°$	0.45% 0.86%
2	$(\sigma_\theta)_{\max} = 3.9$ at $\theta = 327°$ and $270°$ $(\sigma_\theta)_{\min} = -1.691$ at $\theta = 40°$	$(\sigma_\theta)_{\max} = 3.942$ at $\theta = 323.34°$ $(\sigma_\theta)_{\min} = -1.696$ at $\theta = 36.84°$	1.06% 0.29%

Table 3
Maximum tangential stress concentration values obtained from the analytical model and the PGD manifold.

Gap G	Maximum stress concentration factor using the analytical method	Maximum stress concentration factor from the manifold	Relative error
$G = R/4$	5.48	4.82	12%
$G = R/2$	4.035	4.059	0.6%
$G = R$	3.26	3.22	1.2%
$G = 3R/2$	3.1	3.18	2.5%

from Table 2, which also shows that the mutual influence of the holes in a four-hole configuration results in a higher stress concentration than in a two- or three-hole configuration.

As mentioned in the introduction, interesting results using the authors' method have been obtained by [2], particularly results that complement those published by [16], and which further attest to the accuracy of the method.

5. Validation of the manifold

In this section, we compare the results obtained from the analytical model to the results obtained from the reduced-order model manifold for four different relative positions of the considered holes. The results are computed for a radius $R =$ 25 mm and gaps G equal to 6.25 mm, 12.5 mm, 25 mm, and 37.5 mm, which coincides with $G = R/4$, $R/2$, R and $3R/2$. In this section, the computed stress concentration factors are the ratios of the stress along the direction of the load, divided by the same stress that would exist in the plate without holes. The results came as illustrated in Table 3.

The results shown in Table 3 evidence a good correlation between the analytical model and the stress concentration manifold obtained from the model reduction techniques, except for the gap value $G = R/4$. The high relative error appearing for low gap values is eventually generated by the mesh size, unable to reflect the high stress concentration around very close holes. However, the error is still acceptable.

6. Conclusion

In this paper, we develop a numerical strategy to construct a reliable computational vademecum based on the PGD technique. Later on, the results are post-treated to construct a stress concentration manifold that can be used online in real time to assess the danger generated by any hole or defect in a structure. The stress concentration factors are identified by simply looking at the diagram, which can be used by simple technicians without any scientific background, or even by an artificial intelligence decision algorithm. Moreover, the results are validated analytically and through using reliable and industrially proven softwares. To validate the results analytically, a procedure to calculate the tangential stress at any point in an infinite, isotropic plate, under in-plane loading and containing any number of non-intersecting, circular holes of different sizes, and disposed in any manner within the plate, has been developed. The procedure, which is based on Muskhelishvili's complex potential approach coupled with the Schwartz alternating method, is incorporated in a Mathematica program.

On the other hand, the manifold technique developed in this paper can be applied to any simulation-based decision-making algorithm. The applications extend beyond the stress concentration to any real-time simulation-based artificial intelligence decision-making algorithms, which can create the virtual manifold of the risk or a danger coefficient. Finally, the manifold can be stored in a smartphone application and used by simple workers without any scientific background.

Appendix A. The PGD using a geometrical transformation

Considering the weakform of the problem depicted in Eq. (3) under the form:

$$\frac{1}{4}\int_{\Omega}\left(\nabla\mathbf{u}^{*}+\nabla\mathbf{u}^{*\intercal}\right)\cdot\mathcal{K}\cdot\left(\nabla\mathbf{u}^{*}+\nabla\mathbf{u}^{*\intercal}\right)\mathrm{d}\Omega=\int_{\partial\Omega}\mathbf{u}^{*}\cdot\mathbf{F}\mathrm{d}\Omega \tag{16}$$

one may note that the derivation are performed in the physical space $\mathbf{X}=(x,y,z)$, where $\mathrm{d}\Omega=\mathrm{d}x\,\mathrm{d}y\,\mathrm{d}z$. However, the calculation shall be performed in the apparent space $\mathbf{S}=(q,r,s)$. The geometrical transformation depicted in Eq. (4) is used to compute the transformation's derivatives. For instance, we note the Jacobian matrix of the transformation by $\mathbf{J}$, such as:

$$\mathbf{J}=\begin{bmatrix}\frac{\partial x}{\partial q} & \frac{\partial x}{\partial r} & \frac{\partial x}{\partial s}\\ \frac{\partial y}{\partial q} & \frac{\partial y}{\partial r} & \frac{\partial y}{\partial s}\\ \frac{\partial z}{\partial q} & \frac{\partial z}{\partial r} & \frac{\partial z}{\partial s}\end{bmatrix} \tag{17}$$

and define the derivations of the inverse transformations by

$$\mathbf{B}=\begin{bmatrix}\frac{\partial q}{\partial x} & \frac{\partial r}{\partial x} & \frac{\partial s}{\partial x}\\ \frac{\partial q}{\partial y} & \frac{\partial r}{\partial y} & \frac{\partial s}{\partial y}\\ \frac{\partial q}{\partial z} & \frac{\partial r}{\partial z} & \frac{\partial s}{\partial z}\end{bmatrix} \tag{18}$$

In our problem, the transformation is defined by part such as:

$$\mathbf{B}=\sum_{i=1}^{i=5}\sum_{j=1}^{j=3}\phi_{ij}\mathbf{B}_{ij} \tag{19}$$

where the ϕ_{ij} are indication functions for the five transformations in the q dimension and three transformations in the r dimension as per Eq. (4). The matrix $\mathbf{B}_{ij}$ of Eq. (19) is the derivation of the inverse transformation i in dimension q and j in dimension r, while ϕ_{ij} is a characteristic function equal to 1 when both q and r exist in the domains q_i and r_j, $\phi_{ij}=0$ elsewhere.

One may note that the transformations have constant derivatives and are not functions of (q,r,s), which gives an easily separable determinant of the Jacobian of the transformation. Such geometrical mapping increases the separability of the problem, since the inverse transformation and its Jacobian matrix can be easily written in a separated form as a function of the problem's extra coordinates.

We can write the gradient ∇ in the real (x,y,z) domain as a function of the gradient in the transformed domain (q,r,s), noted by $\nabla_{\mathbf{r}}$ such as:

$$\nabla=\mathbf{B}\,\nabla_{\mathbf{r}} \tag{20}$$

Therefore, the weak form of the problem can be written as:

$$\frac{1}{4}\int_{\mathbf{r}}\left(\nabla_{\mathbf{r}}\mathbf{u}^{*}+\nabla_{\mathbf{r}}\mathbf{u}^{*\intercal}\right)^{\intercal}\mathbf{B}^{\intercal}\cdot\mathcal{K}\cdot\mathbf{B}\left(\nabla_{\mathbf{r}}\mathbf{u}^{*}+\nabla_{\mathbf{r}}\mathbf{u}^{*\intercal}\right)\det(\mathbf{J})\,\mathrm{d}\mathbf{r}=\int_{\partial\mathbf{r}}\mathbf{u}^{*}\cdot\mathbf{F}\det(\mathbf{J})\,\mathrm{d}\mathbf{r} \tag{21}$$

The weak form illustrated in Eq. (21) is used for PGD simulation. The interested reader wishing to get the detailed PGD algorithm to obtain the solution in transformed domains may refer to one of the following publications and the references therein [13,12].

Appendix B. The Schwartz alternating process

The Schwartz alternating method as it applies to the multi-hole problem is presented in this section. The method is a stepwise process that cycles over as many calculations as is needed to satisfy the boundary conditions on the periphery of each hole of the plate shown in Fig. 9(a) by superposition of the stresses existing around each corresponding hole in Figs. 9(b) and 9(c).

For clarity, we first introduce the notations that are used subsequently in this section to describe the iterative process.

We define $(s_r)_{ij}^k$, $(s_\theta)_{ij}^k$ and $(s_{r\theta})_{ij}^k$ to be, respectively, the radial, tangential and shear stresses arising around hole i or would-be hole i due to loading around hole j, during iteration k, in a plate containing n holes under remote pressure loading. Similarly, we define $(s_r)_i^0$, $(s_\theta)_i^0$ and $(s_{r\theta})_i^0$, $(i=1,\ldots,n)$, to be, respectively, the radial, tangential; and shear stresses around the would-be hole i in a hole-free plate. Recall that $k=0$ means a plate containing no hole.

Furthermore, let $(\sigma_r)_i^k = \sum_{(j=1)}^{n} (s_r)_{ij}^k$, $(\sigma_\theta)_i^k = \sum_{(j=1)}^{n} (s_\theta)_{ij}^k$ and $(\tau_{r\theta})_i^k = \sum_{(j=1)}^{n} (s_{r\theta})_{ij}^k$, $(i=1,\ldots,n)$. Also, let δ be a small positive number sufficiently close to zero. The process now follows.

First cycle, $k=1$:

Step 1. Apply $(s_r)_{11}^1 = -(s_r)_1^0$ and $(s_{r\theta})_{11}^1 = -(s_{r\theta})_1^0$ around hole 1. Calculate $(s_r)_{21}^1$, $(s_\theta)_{21}^1$ and $(s_{r\theta})_{21}^1$ around the would-be hole 2; $(s_r)_{31}^1$, $(s_\theta)_{31}^1$ and $(s_{r\theta})_{31}^1$ around the would-be hole 3,…, $(s_r)_{n1}^1$, $(s_\theta)_{n1}^1$ and $(s_{r\theta})_{n1}^1$ around the would-be hole n.

Step 2. Apply $(s_r)_{22}^1 = -(s_r)_2^0 - (s_r)_{21}^1$ and $(s_{r\theta})_{22}^1 = -(s_{r\theta})_2^0 - (s_{r\theta})_{21}^1$ around hole 2. Calculate $(s_r)_{12}^1$, $(s_\theta)_{12}^1$ and $(s_{r\theta})_{12}^1$ around the would-be hole 1; $(s_r)_{32}^1$, $(s_\theta)_{32}^1$ and $(s_{r\theta})_{32}^1$ around the would-be hole 3,…, $(s_r)_{n2}^1$, $(s_\theta)_{n2}^1$ and $(s_{r\theta})_{n2}^1$ around the would-be hole n.

Step 3. Apply $(s_r)_{33}^1 = -(s_r)_3^0 - (s_r)_{31}^1 - (s_r)_{32}^1$ and $(s_{r\theta})_{33}^1 = -(s_{r\theta})_3^0 - (s_{r\theta})_{31}^1 - (s_{r\theta})_{32}^1$ around hole 3. Calculate $(s_r)_{13}^1$, $(s_\theta)_{13}^1$ and $(s_{r\theta})_{13}^1$ around the would-be hole 1; $(s_r)_{23}^1$, $(s_\theta)_{23}^1$ and $(s_{r\theta})_{23}^1$ around the would-be hole 2,…, $(s_r)_{n3}^1$, $(s_\theta)_{n3}^1$ and $(s_{r\theta})_{n3}^1$ around the would-be hole n.

⋮

Step n. Apply $(s_r)_{nn}^1 = -(s_r)_n^0 - (s_r)_{n1}^1 - (s_r)_{n2}^1 - (s_r)_{n3}^1 - \cdots - (s_r)_{n(n-1)}^1$ and $(s_{r\theta})_{nn}^1 = -(s_{r\theta})_n^0 - (s_{r\theta})_{n1}^1 - (s_{r\theta})_{n2}^1 - (s_{r\theta})_{n3}^1 - \cdots - (s_{r\theta})_{n(n-1)}^1$ around hole n. Calculate $(s_r)_{1n}^1$, $(s_\theta)_{1n}^1$ and $(s_{r\theta})_{1n}^1$ around the would-be hole 1; $(s_r)_{2n}^1$, $(s_\theta)_{2n}^1$ and $(s_{r\theta})_{2n}^1$ around the would-be hole 2; $(s_r)_{3n}^1$, $(s_\theta)_{3n}^1$ and $(s_{r\theta})_{3n}^1$ around the would-be hole 3,…, $(s_r)_{(n-1)n}^1$, $(s_\theta)_{(n-1)n}^1$ and $(s_{r\theta})_{(n-1)n}^1$ around the would-be hole $(n-1)$.

Next, we calculate $(\sigma_r)_i^1$ and $(\tau_{r\theta})_i^1$, $(i=1,\ldots,n)$. If $\text{Max}\left|(s_r)_i^0 + (\sigma_r)_i^1\right| \le \delta$ and $\text{Max}\left|(s_{r\theta})_i^0 + (\tau_{r\theta})_i^1\right| \le \delta$, where Max denotes the maximum value of an expression and the symbol $|\sim|$ denotes the absolute value, then the solution has converged after the first cycle, and the tangential stress around any hole i in the plate of Fig. 9(a) can be calculated as:

$$(s_\theta)_i^0 + (\sigma_\theta)_i^1, (i=1,\cdots,n) \tag{22}$$

Otherwise, steps 1 through n above are repeated and a second cycle is started where the loads applied on the contours of the holes are those calculated at the end of the first cycle, as follows.

Second cycle, $k=2$:

Step 1. Apply $(s_r)_{11}^2 = -(s_r)_{12}^1 - (s_r)_{13}^1 - \cdots - (s_r)_{1n}^1$ and $(s_{r\theta})_{11}^2 = -(s_{r\theta})_{12}^1 - (s_{r\theta})_{13}^1 - \cdots - (s_{r\theta})_{1n}^1$ around hole 1.

Calculate $(s_r)_{21}^2$, $(s_\theta)_{21}^2$ and $(s_{r\theta})_{21}^2$ around the would-be hole 2; $(s_r)_{31}^2$, $(s_\theta)_{31}^2$ and $(s_{r\theta})_{31}^2$, around the would-be hole 3,…, $(s_r)_{n1}^2$, $(s_\theta)_{n1}^2$ and $(s_{r\theta})_{n1}^2$ around the would-be hole n.

Step 2. Apply $(s_r)_{22}^2 = -(s_r)_{21}^2 - (s_r)_{23}^1 - \cdots - (s_r)_{2n}^1$ and $(s_{r\theta})_{22}^2 = -(s_{r\theta})_{21}^2 - (s_{r\theta})_{23}^1 - \cdots - (s_{r\theta})_{2n}^1$ around hole 2.

Calculate $(s_r)_{12}^2$, $(s_\theta)_{12}^2$ and $(s_{r\theta})_{12}^2$ around the would-be hole 1; $(s_r)_{32}^2$, $(s_\theta)_{32}^2$ and $(s_{r\theta})_{32}^2$ around the would-be hole 3,…, $(s_r)_{n2}^2$, $(s_\theta)_{n2}^2$ and $(s_{r\theta})_{n2}^2$ around the would-be hole n.

Step 3. Apply $(s_r)_{33}^2 = -(s_r)_{31}^2 - (s_r)_{32}^2 - \cdots - (s_r)_{3n}^1$ and $(s_{r\theta})_{33}^2 = -(s_{r\theta})_{31}^2 - (s_{r\theta})_{32}^2 - \cdots - (s_{r\theta})_{3n}^1$ around hole 3.

Calculate $(s_r)_{13}^2$, $(s_\theta)_{13}^2$ and $(s_{r\theta})_{13}^2$ around the would-be hole 1; $(s_r)_{23}^2$, $(s_\theta)_{23}^2$ and $(s_{r\theta})_{23}^2$ around the would-be hole 2,…, $(s_r)_{n3}^2$, $(s_\theta)_{n3}^2$ and $(s_{r\theta})_{n3}^2$ around the would-be hole n.

⋮

Step n. Apply $(s_r)_{nn}^2 = -(s_r)_{n1}^2 - (s_r)_{n2}^2 - (s_r)_{n3}^2 - \cdots - (s_r)_{n(n-1)}^2$ and $(s_{r\theta})_{nn}^2 = -(s_{r\theta})_{n1}^2 - (s_{r\theta})_{n2}^2 - (s_{r\theta})_{n3}^2 - \cdots - (s_{r\theta})_{n(n-1)}^2$ around hole n.

Calculate $(s_r)_{1n}^2$, $(s_\theta)_{1n}^2$, $(s_{r\theta})_{1n}^2$ around the would-be hole 1; $(s_r)_{2n}^2$, $(s_\theta)_{2n}^2$, $(s_{r\theta})_{2n}^2$ around the would-be hole 2; $(s_r)_{3n}^2$, $(s_\theta)_{3n}^2$, $(s_{r\theta})_{3n}^2$ around the would-be hole 3,…, $(s_r)_{(n-1)n}^2$, $(s_\theta)_{(n-1)n}^2$ and $(s_{r\theta})_{(n-1)n}^2$ around the would-be hole $(n-1)$.

Next, we calculate $(\sigma_r)_i^2$ and $(\tau_{r\theta})_i^2$, $(i = 1, \cdots, n)$. If:

$$\text{Max} \left| (s_r)_i^0 + (\sigma_r)_i^1 + (\sigma_r)_i^2 \right| \leq \delta \tag{23}$$

and

$$\text{Max} \left| (s_{r\theta})_i^0 + (\tau_{r\theta})_i^1 + (\tau_{r\theta})_i^2 \right| \leq \delta \tag{24}$$

then the solution has converged after the second cycle and the tangential stress around any hole i in the plate of Fig. 9(a) can be calculated as:

$$(s_\theta)_i^0 + (\sigma_\theta)_i^1 + (\sigma_\theta)_i^2, \quad (i = 1, \cdots, n) \tag{25}$$

Otherwise, the procedure above is repeated for another cycle. The procedure will run for as many cycles as is necessary to satisfy the convergence criterion on δ.

References

[1] J.V. Aguado, D. Borzacchiello, C. Ghnatios, F. Lebel, R. Upadhyay, C. Binetruy, F. Chinesta, A Simulation App based on reduced order modeling for manufacturing optimization of composite outlet guide vanes, Adv. Model. Simul. Eng. Sci. 4 (1) (2017) 1–26.
[2] G. Asmar, E. Chakar, T. Jabbour, Some unexpected results in the stress calculation around multiple holes in an isotropic plate under in-plane-loads, in: Proceedings of the 12th Biennial ASME Conference on Engineering Systems Design and Analysis, Copenhagen, Denmark, 2014.
[3] B. Bognet, Stratégie numériques avancées pour la simulation de modeles définis sur une géométrie de plaques et coques: solution 3D avec une complexité 2D, PhD thesis, École centrale de Nantes, 2013.
[4] F. Bordeu, C. Ghnatios, D. Boulze, B. Carles, D. Sireude, A. Leygue, F. Chinesta, Parametric 3D elastic solutions of beams involved in frame structures, Adv. Aircr. Spacecr. Sci. 2 (3) (2015) 233–248.
[5] N. Bur, P. Joyot, C. Ghnatios, P. Villon, E. Cueto, F. Chinesta, On the use of model order reduction for simulating automated fibre placement processes, Adv. Model. Simul. Eng. Sci. 3 (2016) 1–18.
[6] F. Chinesta, A. Ammar, E. Cueto, Recent advances in the use of the proper generalized decomposition for solving multidimensional models, Arch. Comput. Methods Eng. 17 (4) (2010) 327–350.
[7] E. Cueto, C. Ghnatios, F. Chinesta, N. Monte, F. Sanchez, A. Falco, Improving computational efficiency in LCM by using computational geometry and model reduction techniques, Key Eng. Mater. 611 (2014) 339–343.
[8] C. Farhat, P. Geuzaine, G. Brown, Application of a three-field nonlinear fluid-structure formulation to the prediction of the aeroelastic parameters of an F-16 fighter, Comput. Fluids 32 (2003) 3–29.
[9] P. Geuzaine, G. Brown, C. Harris, C. Farhat, Aeroelastic dynamic analysis of a full F-16 configuration for various flight conditions, AIAA J. 41 (2003) 363–371.
[10] C. Ghnatios, Modélisation avancée des procédés thermiques rencontrés lors de la mise en forme des composites, PhD thesis, École centrale de Nantes, October 2012.
[11] C. Ghnatios, A. Ammar, A. Cimetiere, A. Hamdouni, A. Leygue, F. Chinesta, First steps in the space separated representation of models defined in complex domains, in: ASME 2012 11th Biennial Conference on Engineering Systems Design and Analysis, American Society of Mechanical Engineers, 2012, pp. 37–42.
[12] C. Ghnatios, C. Mathis, F. Chinesta, Poroelastic properties identification through micro indentation modeled by using the proper generalized decomposition, in: 3rd International Conference on Advances in Computational Tools for Engineering Applications, ACTEA, IEEE, 2016, pp. 141–145.
[13] C. Ghnatios, C.H. Mathis, R. Simic, N.D. Spencer, F. Chinesta, Modeling soft permeable matter with the proper generalized decomposition (PGD) approach, and verification by means of nanoindentation, Soft Matter 13 (2017) 4482–4493.
[14] C. Ghnatios, G. Xu, A. Leygue, M. Visionneau, F. Chinesta, A. Cimetière, On the space separated representation when addressing the solution of PDE in complex domains, Discrete Contin. Dyn. Syst., Ser. S 9 (2) (2016) 475–500.
[15] D. Gonzalez, J.V. Aguado, E. Cueto, E. Abisset-Chavanne, F. Chinesta, kPCA-based parametric solutions with the PGD framework, Arch. Comput. Methods Eng. 25 (1) (2018) 69–86.
[16] R.A.W. Haddon, Stresses in an infinite plate with two unequal circular holes, Q. J. Mech. Appl. Math. 20 (3) (1967) 277–291.
[17] R.C.J. Howland, Stresses in a plate containing an infinite row of holes, Proc. R. Soc. Lond. Ser. A, Math. Phys. Sci. 148 (864) (1935) 471–491.
[18] R. Ibanez, E. Abisset-Chavanne, J.V. Aguado, D. Gonzalez, E. Cueto, F. Chinesta, A manifold learning approach to data driven computational elasticity and inelasticity, Arch. Comput. Methods Eng. 25 (1) (2018) 47–57.
[19] R. Ibanez, D. Borzacchiello, J.V. Aguado, E. Abisset-Chavanne, E. Cueto, P. Ladeveze, F. Chinesta, Data-driven non-linear elasticity: constitutive manifold construction and problem discretization, Comput. Mech. 60 (5) (2017) 813–826.
[20] G.B. Jeffery, Plane stress and plane strain in bipolar co-ordinates, Philos. Trans. R. Soc. Lond. Ser. A 221 (1921) 265–293.
[21] C.B. Ling, On the stresses in a plate containing two circular holes, J. Appl. Phys. 19 (1948) 77–82.
[22] N.L. Muskhelishvili, Some Basic Problems of the Mathematical Theory of Elasticity, 4th edition, Springer Science, 1977.
[23] S.T. Roweis, L.K. Saul, Nonlinear dimensionality reduction by locally linear embedding, Science 290 (December 2000) 2323–2326.
[24] B. Scholkopf, A. Smola, K.R. Muller, Non linear component analysis as a kernel eigenvalue problem, Neural Comput. 10 (5) (March 2006) 1299–1319.
[25] K. Ting, K.T. Chen, W.S. Yang, Applied alternating method to analyse the stress concentration around interacting multiple circular holes in an infinite domain, Int. J. Solids Struct. 36 (1998) 533–556.
[26] K. Ting, K.T. Chen, W.S. Yang, Stress analysis of the multiple circular holes with the rhombic array using alternating method, Int. J. Press. Vessels Piping 76 (1999) 503–514.